An integrated and homogenized global surface solar radiation dataset and its reconstruction based on a convolutional neural network approach

Boyang Jiao[1,#], Yucheng Su[2], Qingxiang Li*[1,#], Veronica Manara[3],Martin Wild[4]

[1]School of Atmospheric Sciences, Sun Yat-sen University, and Key Laboratory of Tropical Atmosphere−Ocean System, Ministry of Education, Zhuhai 519082, China

[2]Meteorological Bureau of Zhuhai, Zhuhai 519082, China

[3]Department of Environmental Science and Policy, Università degli Studi di Milano, via Celoria 10, 20133, Milano, Italy

[4]Institute for Atmospheric and Climate Science, ETH Zurich, Zurich, Switzerland

[#]Southern Laboratory of Ocean Science and Engineering (Guangdong Zhuhai), Zhuhai 519082, China

Correspondence to: Qingxiang Li (liqingx5@mail.sysu.edu.cn)

Abstract

Surface solar radiation (SSR) is an essential factor in the flow of surface energy, enabling accurate capturing of long-term climate change and understanding the energy balance of Earth's atmosphere system. However, the long-term trend estimation of SSR is subjected to significant uncertainties due to the temporal inhomogeneity and the uneven spatial distribution of the *in-situ* observations. This paper develops an observational integrated and homogenized global-terrestrial (except for Antarctica)) stational SSR dataset ($SSRIH_{station}$) by integrating all available SSR observations, including the existing homogenized SSR results. The series is then interpolated in order to obtain a $5°\times5°$ resolution gridded dataset ($SSRIH_{grid}$). On this basis, we further reconstruct a long-term (1955-2018) global land (except for Antarctica) SSR anomalies dataset with a $5°\times2.5°$ resolution ($SSRIH_{20CR}$) by training improved partial convolutional neural network deep learning methods based on the reanalysis 20CRv3. Based on this, we analysed the global land (except for Antarctica) /regional scale SSR trends and spatiotemporal variations: the reconstruction results reflect the distribution of SSR anomalies and have high reliability in filling and reconstructing the missing values. At the global land (except for Antarctica) scale, the decreasing trend of the $SSRIH_{20CR}$ (-1.276 ± 0.205 W/m^2 per decade) is slightly smaller than the trend of the $SSRIH_{grid}$ (-1.776 ± 0.230 W/m^2 per decade) from 1955 to 1991. The trend of $SSRIH_{20CR}$ (0.697 ± 0.359 W/m^2 per decade) from 1991 to 2018 is also marginally lower than that of the $SSRIH_{grid}$ (0.851 ± 0.410 W/m^2 per decade). At the regional scale, the difference between the $SSRIH_{20CR}$ and $SSRIH_{grid}$ is more significant in years and areas with insufficient coverage. Asia, Africa, Europe and North America cause the global dimming of the $SSRIH_{20CR}$, while Europe and North America drive the global brightening of the $SSRIH_{20CR}$. Spatial sampling inadequacies have largely contributed to a bias in the long-term variation of global /regional SSR. This paper's homogenized gridded dataset and the Artificial Intelligence reconstruction gridded dataset (Jiao and Li, 2023) are all available at https://doi.org/10.6084/m9.figshare.21625079.v1.

1 Introduction

Energy flows at the Earth's surface play an essential role in climate change and human activity and link to physical processes such as global warming, glacier retreating, hydrological cycle, and carbon budget (Hoskins and Valdes, 1990; Peixoto et al., 1992; Trenberth and Fasullo, 2013; Wild, 2012). As a critical factor characterizing surface energy flows, Surface Solar Radiation (SSR) largely determines the climatic conditions and ecological environment in which we live. Therefore, a more accurate and comprehensive analysis of the SSR fluxes will help better understand the Earth's atmospheric system. *In-situ* observations provide the most accurate baseline data for measuring SSR. They allowed for the first time the detection of decadal changes in SSR known as "dimming and brightening" (Wild et al., 2005), especially considering that they cover a longer period concerning another type of data like for example satellite data (Pfeifroth et al., 2018). Even observational data often have uneven distribution and missing data with respect to the satellite data, especially in areas with complex orography (Manara et al., 2020).

The sources of *in-situ* SSR observations are mainly collected from the Global Energy Balance Archive (GEBA) (Wild et al., 2017) and the World Radiation Data Centre (WRDC) (Tsvetkov et al., 1995). Furthermore, other SSR station series are obtained from the high quality Baseline Surface Radiation Network (BSRN) (Driemel et al., 2018) and the data centres of individual national hydrometeorological services. However, two issues still need to be addressed: 1) the inhomogeneity of station data resulting from station relocations and instrumentation changes severely impacts the climate change assessment. For the regions with a relatively high density of stations, like Europe (Manara et al., 2019; Manara et al., 2016; Sanchez-Lorenzo et al., 2013a; Sanchez-Lorenzo et al., 2015; Sanchez-Lorenzo et al., 2013b), Japan (Ma et al., 2022) and China (Ju et al., 2006; Wang, 2014; Wang et al., 2015; Wang and Wild, 2016; Yang et al., 2018b; You et al., 2013), much previous work has redefined the degree and timing of "dimming and brightening" by addressing the inhomogeneity of the SSR data series. For example, in Spain, the average annual homogenized SSR series has a significant increasing trend (+ 3.9 W/m^2 per decade) during the 1985–2010 period (Sanchez-Lorenzo et al., 2013a). The period of dimming observed in Italy's homogenized SSR series is not apparent in the 1960s and early 1970s when the raw series (inhomogenized) are taken into account (Manara et al., 2016). The direct measurements of SSR show a level trend from 1961 to 2014 over Japan, while their homogenization series display a decreasing trend (0.8-1.6 W/m^2 per decade) (Ma et al., 2022). In China, homogenization largely eliminated the dramatic

69   non-climatic rise of the early 1990s and also reduced the increasing trend from 1990 to 2016 (Yang et

70   al., 2018b). However, most of the research was still limited to regional scales. 2) The issue of limited

71   spatial sampling of long observational stations and their uneven distribution especially over areas with

72   complex orography. Considerable efforts have been devoted to filling in /interpolating the missing values

73   in climate datasets ("spatial analysis") (Collins, 1996; Erxleben et al., 2002; Scudiero et al., 2016). The

74   traditional spatial interpolation methods commonly used include Inverse Distance Weighted (Fisher et

75   al., 1993; Shepard, 1968), Kriging (Krige, 1951), Thin-Plate Splines (Bookstein, 1989) et cetera. Since

76   the 1980s, physical parametric interpolation (Feng and Wang, 2021; Tang et al., 2019) and Bayesian

77   fusion schemes (Aguiar et al., 2015) based on multi-source observational data were widely used, when

78   the emergence of highly accurate and relatively precise satellite data. However, the resulting fusion

79   datasets cover a too short period to investigate their decadal and multi-decadal variations and to study

80   the underlying causes. The spatial, temporal, and spectral coverage of a single satellite is limited, and

81   multiple satellite data are therefore often used in tandem with each other; however, such a

82   discontinuity in time and space can introduce inhomogeneity into a dataset (Evan et al., 2007; Feng

83   and Wang, 2021; Shao et al., 2022). Reanalysis products are an important complement containing

84   long-term SSR data, therefore have been widely used in climate studies (Huang et al., 2018; Jiao et

85   al., 2022; Urraca et al., 2018; Zhou et al., 2018a; Zhou et al., 2017) due to the dynamically consistent

86   and spatiotemporally complete atmospheric fields with high resolution and open access to data.

87   However, existing studies have shown that reanalysis products generally overestimate multi-year

88   mean SSR values compared to observations over land (He et al., 2021). With the continuous

89   development of climate system simulations, model data from the Coupled Model International

90   Program (CMIP) have become an important resource for conducting climate change research (Gates

91   et al., 1999; Zhou et al., 2019). Previous studies have shown that the models used in CMIP6

92   overestimate the global mean SSR (He et al., 2023; Jiao et al., 2022; Wild, 2020). The rise of deep

93   learning and big data techniques has brought about an explosion of artificial intelligence (AI). Machine

94   learning is increasingly being used in spatial interpolation, such as the spatial reconstruction of surface

95   temperature datasets (Huang et al., 2022; Kadow et al., 2020; Cao et al., 2022), the spatial and temporal

96   reconstruction of turbulence resolution (Fukami et al., 2021), etc. Furthermore, it shows high accuracy

97   and low uncertainty in reproducing and predicting SSR (Leirvik and Yuan, 2021; Tang et al., 2016; Yang

98   et al., 2018a; Yuan et al., 2021). However, long-term homogenized SSR datasets with global terrestrial

99 coverage have yet to be developed, resulting in significant uncertainties in assessing global SSR variation

100 (Jiao et al., 2022).

101   Therefore, developing a more homogeneous and comprehensive global long-term SSR climatic dataset

102 that provides a better benchmark for observational constraints on the global surface energy balance

103 /budget remains a valuable and challenging task. This paper first homogenizes and grids the most

104 extensive collection of available global SSR station observations. Then, the missing grid boxes /years

105 are spatially interpolated using a convolutional neural network (CNN) approach to obtain a globally

106 covered land surface SSR anomalies dataset. Finally, the reconstructed datasets are initially analysed and

107 evaluated. Thus, the paper is divided into seven main sections. The data resources are introduced in

108 Section 2. Section 3 presents the data homogenization, and the CNN model reconstruction methods. The

109 data homogenization and verification are shown in Section 4. Section 5 gives the AI reconstruction results.

110 Section 6 is the availability of the datasets. Conclusions are provided at the end of the paper.

111 **2 Data**

112 Nine SSR datasets are collected to derive the global SSR variable. In particular, six datasets contain data

113 from observational stations (Section 2.1): two global ground-based measurement datasets (GEBA,

114 WRDC) and four homogenized products at regional and country levels (Europe, China, Japan and Italy).

115 Three of the adopted datasets are reanalysis data (Section 2.2.1): Fifth generation European Centre for

116 Medium-Range Weather Forecasts (ECMWF) reanalysis (ERA5), 20th Century Reanalysis version 3

117 (20CRv3) reanalysis data and the Coupled Model Intercomparison Project Phase 6 (CMIP6) historical

118 simulation output (125). Specifically, the ERA5 data are used to fill the data over oceans and Antarctica

119 (Section 3.2.1), 20CRv3 data and CMIP6 simulations are used for the AI model training (Section 5.1)

120 and reconstruction. All have been listed in Table 1.

121 **2.1 In situ observational Data**

122 **2.1.1 Global datasets**

123 There are two main sources of raw SSR data (see Table 1): the ETH Zurich GEBA with monthly data

124 from 2,445 globally distributed stations, starting from 1922 until 2020, and the WRDC dataset with

125 monthly globally distributed data from 1136 stations since 1964. The first one is available for download

126 at https://geba.ethz.ch (Last access: 2022.7. 2). The second one published the first SSR radiation balance

127 data in 1965 and then its publication has been issued four times a year since 1993 and is available for

128 download at http://wrdc.mgo.rssi.ru/ (Last access: July 2021).

2.1.2 National (regional) homogenized station datasets

130 1) Chinese homogenized SSR dataset

131 The China Meteorological Radiation Fundamental Elements Monthly Value Data Set has been

132 downloaded at http://www.nmic.cn. The homogenized SSR dataset in China is released by the National

133 Meteorological Information Centre (NMIC), China Meteorological Administration (CMA) (Yang, 2016).

134 The data are available for the period between Jan 1950 to Dec 2014, and the follow-up data are extended

135 with raw observations from NMIC. They used the sunshine duration (SSD) data from nearby stations to

136 construct an arguably better reference to identify inhomogeneities in the SSR data. Then, a combined

137 metadata and the maximum penalty t-test (PMT) method was used to detect the change points. Finally,

138 they were adjusted by a quantile matching (QM) algorithm (Wang and Feng, 2013). The final

139 homogenized SSR station dataset was converted to gridded data using the first difference method (FDM

140 (Peterson et al., 1998)) and is available for download at http://www.nmic.cn. Last Access: September

141 2022.

142 2) Japanese homogenized SSR dataset

143 Ma et al. (Ma et al., 2022) released a Japanese SSR homogenized dataset in 2022 spanning the period

144 between 1870 and 2015. First, they homogenized SSD based on PMF (penalized maximal F test) and

145 QM algorithms. They then used the homogenized SSD from the previous step as a reference series,

146 combined with metadata and PMT, to detect change points. Finally, they adjusted the change points by

147 the QM algorithm. For more details on data descriptions, the adopted methodology and downloading

148 data refer to https://data.tpdc.ac.cn/en/data/45d73756-3f5a-4d27-82a4-952e268c20e8/, Last Access:

149 March 2022.

150 3) European homogenized SSR data

151 A homogenized dataset of European SSR stations was developed by Sanchez-Lorenzo et al. (Sanchez-

152 Lorenzo et al., 2015) and is currently available as a full public download at

153 https://agupubs.onlinelibrary.wiley.com/doi/full/10.1002/2015JD023321. They selected the 56 longest

154 Central European SSR series available in GEBA dataset with data for the period comprised between

155 1922 and 2012. They adjusted them to ensure temporal homogeneity homogenizing the data with the

156 Standard Normal Homogeneity Test (Alexandersson, 1986) and the Craddock test (Craddock, 1979).

157 4) Italian homogenized SSR dataset

158 The Italian homogenized SSR datasets are those published by (Manara et al., 2019; Manara et al.,

159 2016). As candidate stations to use as reference series, they selected the ten series located in the same

160 area of the series to be tested and that series correlate well with the test one. In particular, they tested the

161 change points with the Craddock test (Manara. et al., 2017) and when a break is identified by more than

162 one reference series the preceding portion of the series is corrected, leaving the most recent portion

163 unchanged. In this way, the SSR stations were homogenized, and then the missing values were

164 interpolated.

165 **2.2 Other datasets**

166 **2.2.1 Reanalysis**

167 ERA5 can be used to fill in SSR data from the oceans and Antarctica and carry out the global

168 reconstruction, taking into account its high spatial resolution and reliable performance of SSR (Jiao et

169 al., 2022; Liang et al., 2022). After the reconstruction, we removed the data for the ocean reanalysis and

170 maintain the data only in the land area (except for Antarctica). In addition, two SSR data products

171 (20CRv3, CMIP6) are used to train AI models. These are:

172 1) ERA5 (space-filling data): ERA5 is the fifth generation of the European Centre for Medium-Range

173 Forecasting reanalysis product, which currently publishes data from 1950 to the present (Hersbach et al.,

174 2020). In addition, ERA5 has an hourly output and an uncertainty estimate from the ensemble. The data

175 is based on the Integrated Forecasting Model Cy41r2 run in 2016, which contains a 4D-Var assimilation

176 scheme. In ERA5, SSR is obtained from a Rapid Radiation Transfer Model (RRTM) (Mlawer et al.,

177 1997). The present study utilizes monthly SSR data for the period 1955-2018 from ERA5 with a

178 resolution of $0.25\degree \times 0.25\degree$ (last accessed in July 2022). It can be downloaded at

179 https://cds.climate.copernicus.eu

180 2) 20CRv3 (data for AI model training): The 20CR Project is an effort led by NOAA's Physical

181 Sciences Laboratory and CIRES at the University of Colorado, supported by the Department of Energy,

182 to produce reanalysis datasets spanning the entire 20th century and much of the 19th century (Slivinski

183 et al., 2019). 20CR provides a comprehensive global atmospheric circulation data set from 1850 to 2015.

184   Its chief motivation is to provide an observational validation dataset, with quantified uncertainties, for

185   assessing climate model simulations of the 20th century. 20CR uses an ensemble filter data assimilation

186   method which directly estimates the most likely state of the global atmosphere every three hours and

187   estimates the uncertainty in that analysis. The most recent version of this reanalysis, 20CRv3, provides

188   8-times daily estimates of global tropospheric variability across 75 km grids, spanning 1836 to 2015

189   (with an experimental extension from 1806 to 1835). The present study uses monthly SSR data of

190   20CRv3 (NOAA /CIRES /DOE 20CR, 80 members) from 1955-2015. We selected all 80 members of

191   the 20CR as input (1 for evaluation and to test reconstruction, the other 79 for training the CNN model).

192   The SSR of 20CRv3 has a spatial resolution of 0.7°×0.7° (Last accessed: May 2022). The download is

193   available at https://portal.nersc.gov/archive/home/projects/incite11/.

194   **2.2.2 CMIP6 models output**

195   3) CMIP6 models output (data for AI model training): the Coupled Model Intercomparison Project,

196   driven by the World Climate Research Program, is now in its 6th phase. Specifically, CMIP6 is

197   considered as the current state of the art way of producing future climate simulations, including predicting

198   future SSR based on different climate scenarios (Zhou et al., 2018b). It provides an important resource

199   for studying current and future climate change (Eyring et al., 2016). The historical simulations of CMIP6

200   are designed to reproduce observed climate and climate change, constrained by radiative forcing. Its

201   historical simulation spans between 1850 and 2014. In this study, we selected 125 members out of a total

202   of 507 members from several CMIP6 large ensemble models (with more than 10 realizations/runs) with

203   high correlation coefficients with observations as input to train and validate the CNN model (1 for

204   evaluation and to test reconstruction, the other 124 for training the CNN model). We selected the monthly

205   downward shortwave radiation from 1955 to 2014 (see Table S1 in the Supplemental Material (SM)).

206   Last access July 2022. Download at: https://esgf-node.llnl.gov/search/cmip6.

3 Methods

3.1 Data Quality Control (QC) and homogenization

The SSR data homogenization method is only applied to the two inhomogenized *in-situ* observations datasets (GEBA and WRDC). The Quality Control (QC) and homogenization flowchart (Figure 1) is divided into three steps: 1. QC; 2. Homogenization; 3. Integration and consolidation.

3.1.1 QC

The QC of SSR data includes the following steps:

1) Simple integration: integration of the GEBA (2445) and WRDC (1136) datasets removing stations with no data and leaving 2681 stations.

2) Removing duplicate stations: a. Stations with similar latitude and longitude. We consider two stations with totally identical latitude and longitude to be the same station; b. Stations less than 10km apart. We averaged the duplicate stations in this a and b case; c. Special duplicate stations: Stitching together data of the duplicate stations based on metadata from CMA.

3) Remove stations or years /months for which a climatic analysis cannot be established: we remove stations with records of less than ten years and values more than three times (3σ criterion (Olanow and Koller, 1998) the standard deviation of the SSR anomalies.

4) Candidate stations (487) with a record length greater than 15 years in the period 1971-2000 are selected. We added stations (715) with more than 10 years of SSR records to increase the number of available stations for a better homogenization of the candidate stations (Figure 2).

3.1.2 Station series homogenization

This paper uses the RHtestV4 software package to test and adjust the SSR station data for homogeneity (http://etccdi.pacificclimate.org/software.shtml) (Wang and Feng, 2013). The package is based on the empirical penalty functions PMF (Wang, 2008b) and PMT (Wang, 2008a; Wang et al., 2007) for the homogenization test. It takes into account the lag-1 autocorrelation of the time series. It embeds a multiple linear regression algorithm to significantly reduce the problem of an unbalanced distribution of pseudo-identification rates and test efficacy. Also, RHtestV4 uses the QM algorithm (Vincent et al., 2012; Wang et al., 2010) and Mean-Adjustments to adjust the identified change points.

The specific steps are as follows:

235 1) Building the reference series

236 a. We processed the data from all stations series (715) into the annual first differences (FD) series

237 e_i(Eq. (1)) (Peterson et al., 1998).

238 b. We calculated the correlation of the annual FD series between the series from the potential reference

239 pool and the candidate stations.

240 c. We calculated the distance between the potential reference pool stations and candidate stations.

241 d. We selected potential stations according to the correlation coefficient (CC >= 0.6) between the series

242 from potential reference pool and candidate stations. And the potential stations also satisfy the limits in

243 distances (<= 500km) between the potential pool stations and candidate stations.

244 e. We obtain the reference FD series (Re)based on the m potential reference series (Pe$_i$) and the CCs

245 (c_i) between the potential reference series (Pe$_i$) and candidate stations series (Eq. (2)).

246 f. The synthesized reference FD series (Re) (Eq. (2)), plus the average of all potential reference series

247 ($\bar{R}$), yields the final annual reference series (R) (Eq. (3)).

$$e_i = x_i - x_{i+1}$$

$$\text{i=1, 2, …, n-1} \qquad (1)$$

$$R_e = \frac{\sum_{i=1}^{m} Pe_i * c_i^2}{\sum_{i=1}^{m} c_i^2} \qquad (2)$$

$$R = R_e + \overline{R} \qquad (3)$$

248 e_i Annual FD series,

249 x_i Raw observational station SSR in the year i,

250 Re Final reference series,

251 Pe_i Potential reference series,

252 c_i CC between the potential reference series and the candidate stations series.

253 2) Testing and adjusting the candidate series

254 The homogenization test algorithm used in this paper is the PMT. This method is a reference series-

255 dependent test for a normalized candidate series. It assumes that the linear trend of the time series is zero

256 and uses the degree of mean deviation at different points in the series to find change points. Furthermore,

257 it eliminates the effect of different sample lengths on the test results. At the same time, the method

258 introduces an empirical penalty factor, which effectively improves detection. We used the PMT to test

259 the homogeneity of the candidate series based on the reference series established in 1). We then adjusted

260   the statistically significant(p>0.05) changepoints obtained using the mean adjustment method (p>0.05).

261   We homogenize the monthly series for 66 stations (see Figure S1 in the SM).

262   **3.1.3 Integration and consolidation**

263   As can be seen from Figure 1, the candidate stations (487) are relatively sparse. To better adapt deep

264   learning methods for the dataset reconstruction later, we adjusted, added and integrated station series

265   based on the results of homogenized data from other scholars: 1) We added stations with more than 10a

266   overall (1955-2018) records but no more than 15a during the 1971-2000 period, and removed those

267   stations that were clearly inhomogeneous (25) and some years of the station (3); 2) We subsequently

268   integrate monthly SSR series for 116 stations based on the results of homogenization by other scholars

269   (China (56), Japan (8), Europe (2) and Italy (50)). After the above steps, we end up with a homogenized

270   dataset containing 944 stations (Figure 3). The details of the processing and classification are shown in

271   Table S2 (see in the SM).

272   **3.2 CNN model reconstruction methods**

273   The CNN deep learning model network architecture uses a U-shaped structure similar to the U-net

274   (Ronneberger et al., 2015). The advantage of using this model is: 1) both high and low-frequency

275   information of the picture can be retained, and when reconstructing the SSR data, not only the grid point

276   information close to the missing measurement point will be considered, but also information from more

277   distant locations (which may be remotely correlated with that missing measurement point); 2) This makes

278   the model convergence faster and more economical in terms of computational resources. The upper part

279   of the U-shaped structure, which has no down samples or a low number of down samples, represents the

280   high-frequency information of the graph. These sections contain much of the detail in the graph and the

281   relationships between similar grid points are conveyed by this section. The lower half of the U-shaped

282   structure is down-sampled more often and represents the lower frequency information of the graph. The

283   global radiation of a wide range of undulations is transmitted by it, and then the information at the various

284   levels of the U-shaped structure is connected and transmitted through the skip connection, allowing the

285   whole network to remember all the information of the picture very well. The model uses nearest

286   neighbour upsampling in the decoding phase, the skip links will concatenate two feature maps and two

287   masks as the feature and mask inputs for the next part of the convolution layer. The input to the last part

288 of the convolution layer will contain the original input image concatenated with the holes and the original

289 mask, allowing the model to replicate the gap-free pixels. The complex and variable nature of the sea-

290 land boundary then has a significant impact on the reconstruction, when we reconstruct the global land

291 SSR data. Therefore, we use partial convolution at the image boundaries with a suitable image padding,

292 ensuring that the padding content at the image boundaries is not affected by values outside the image.

293 The deep learning models' convolutional layers and loss functions have been described in the SM.

294   We further reconstruct a long-term (1955-2018) global SSR anomalies dataset ($SSRIH_{20CR}$) by using

295 improved partial CNN deep learning methods based on a "perfect" dataset. CNN consists of three parts.

296 A convolutional layer to reduce the number of weights by extracting local features, a pooling layer to

297 reduce peacekeeping and prevent overfitting, and a fully connected layer to output the desired result. In

298 this paper, a modified CNN network is used to model the reconstruction of the SSR data, with the

299 convolutional layer replaced by a partial convolution method and mask update. This method is the latest

300 in image restoration effects and can restore irregular holes, an advantage over other image restoration

301 methods that can only restore rectangular holes. Therefore, this paper uses the modified CNN model

302 (Kadow et al., 2020) to recover the missing part of the global terrestrial SSR (except Antarctica). The

303 specific reconstruction steps and processes are as in Figure 4.

304 **3.2.1 Data pre-processing**

305 The homogenized station data is converted to grid box anomalies using the Climate Anomalies Method

306 (CAM) (Jones et al., 2001). CAM is a commonly used method for converting station anomaly data to

307 gridded data. We divide all global areas into a $5° \times 5°$ grid, after which we calculate the SSR anomalies

308 (relative to 1923-2020) within the grid box by averaging the anomalies of all stations (at least 1 station

309 in it). If there are more than one site exists in the same grid box, the record length of this grid box is the

310 total length of all sites in that grid box. Finally, we removed the values that were more than three times

311 the standard deviation of the SSR anomaly time series after gridding. SSRs are all processed as daily

312 average anomalies, i.e., monthly anomalies divided by 30 (each month is approximated as 30 days). We

313 multiplied all the values by 30 again when the reconstruction is complete. The global land (except for

314 Antarctica) distribution and coverage of SSRs after gridding are shown in Figure 5 a, b.

315   As seen in Figure 5a, the SSR is spatially sparsely distributed across South America and Africa. As

316 shown in Figure 5b, SSR coverage increased yearly from 1950 until the mid-1970s, when it slowly

317 decreased. In 2013, the coverage rate decreased sharply due to untimely data submission. Considering

318 the SSR coverage above, we only kept the years (1955-2018) with data coverage of more than 8% of

319 global land (except for Antarctica) areas.

320   Comparisons show that the ERA5 has high spatial resolution and relatively reliable performance in

321 the temporal variations and long-term trends (Liang et al., 2022; Jiao et al., 2022). To obtain a higher

322 data coverage and ensure that the AI model runs well, we used the ERA5 to fill the SSR of homogenized

323 global gridded SSR in the Antarctic and ocean areas. However, if we use the SSR of ERA5 to directly

324 fill the SSR of homogenized global gridded SSR (SSRIH$_{grid}$) in the Antarctic and on the ocean areas,

325 then the relatively weaker ocean SSR variations (variabilities, decadal changes, trends, etc.) from ERA5

326 will inevitably introduce certain systematic biases in land SSR reconstruction due to the SSRs have the

327 lower coverage on the land. Therefore, we designed an algorithm to avoid excessive diffusion of SSR

328 system bias in terrestrial areas: we first calculated the ratios γ_i ($i=1, 2, 3, ..., n$) between the SSR from

329 ERA5 and from SSRIH$_{grid}$ on the land in all n years. For a single grid box, the γ_i have small changes

330 and are regarded as a constant γ_{median} (Eq (4)), and the γ_{median} vary by latitude and longitude both on

331 the marine and the land areas. We then extrapolated the γ_{median} for all the grid boxes along the land

332 and sea boundaries. If there is no observation there, then the adjacent ocean ERA5 SSR is used to take

333 its place after it is adjusted according to the differences between the SSR variations (represented by the

334 linear trends) for the different underlying surfaces (Eq (5).

$$\gamma_{median} = Median(\frac{OBS_{i\_land}}{ERA5_{i\_land}}), \tag{4}$$

$$OBS_{i\_O\&L}(land) = ERA5_{i\_O\&L}(Ocean) * \gamma_{median} * \frac{T_O}{T_L}, \tag{5}$$

$$i = 1,2,3......,n$$

335   γ_{median}: The median value of the ratios of OBS and ERA5 land SSR series,

336   OBS_{i_land}: Land SSR for the year i from SSRIH$_{grid}$ in a single grid,

337     $ERA5_{i\_land}$: Land SSR for the year i from ERA5in a single grid,

338     $OBS_{i\_O\&L}(land)$: LandSSRalong the sea-land boundary(land) for the year i from SSRIH$_{grid}$,

339     $ERA5_{i\_O\&L}(Ocean)$: Ocean SSR along the sea-land boundaryfor the year i from ERA5,

340   T_O: Trend of ERA5 SSR on ocean areasin all n years,

341   T_l: Trend of ERA5 SSR on areas in all n years.

3.2.2 AI Model reconstruction

We use a server (configured with processor Intel (R) Core (TM) i7-8700 CPU @ 3.20GHz 3.19 GHz, RAM 32G, 64-bit OS, GPU model 516.94, NVIDIA GeForce 1080T version, Python 3.9.12 64-bit, CUDA 10.1) for AI models training. The specific training steps are as follows:

1) A total of 768 missing value masks (monthly masks between 1955 and 2018) were prepared for training and validation using '1' for existing and '0' for missing values;

2) The 20CRv3 /CMIP6 training set (monthly values between 1955 and 2015 /2014) and missing value masks are fed into the 20CR-AI /CMIP6-AI model for training;

3) We perform 1,500,000 training sessions with an interval of 10,000 sessions for the training output model.

Afterwards, the two AI models are validated against the root mean squared error (RMSE) /CCs of the reconstructed SSRs (SSR$_{20CR}$/SSR$_{CMIP6}$). The validation set SSRs, and the optimal number of training cycles is 1,100,000 (see Figure S2, Figure S3 and Figure S4 in the SM). The initial hyper-parameters of the model are set as follows; learning rate of 2e-4 and learning finetune of 5e-5. First, we set the batch size to 16 in the first 500000 iterations and fine-tuned it to 18 in the last 10000000 iterations, for a total of 1500000 iterations, to suppress the overfitting phenomenon generated during the training process, and validate the model every 10000 times and early stopping if the validation shows a decreasing trend, the final number of training times used is 1100000. Second, L2 regularization is also added to regulate the loss function (see Eq. (9) in the SM).

The training result models generated by the different AI models are obtained separately for the different training sets. The model is first used to reconstruct a reanalysis validation set with the same missing value mask as the original observation dataset. This is followed by a validation of the reconstruction against the original reanalysis dataset (calculation of CC and RMSE) to understand the discrepancies in the model reconstruction.

4 Data homogenization and verification

We homogenized the original monthly stations /gridded SSR time series (SSRIH$_{station}$ /SSRIH$_{grid}$) using the method in section 3.1.2. We selected six continental regions, excluding Antarctica and the Arctic, from the eight continents of the world defined by Xu et al. (Xu et al., 2018) (Asia, Africa, South America,

370   Europe, North America, Australia, Antarctica and the Arctic). The decreasing trend of the SSRIH$_{grid}$ is

371   consistent with the original gridded SSR series (SSRI$_{grid}$) during 1955-1991 while the increasing trend

372   during 1991-2018 is weaker. At the regional scale, the SSRIH$_{grid}$ has a generally similar variation to the

373   SSRI$_{grid}$, and the SSRIH$_{grid}$ usually more representative of climate change than SSRI$_{grid}$ at individual

374   stations.

375   Figure S5 (see in the SM) illustrates the long-term variations of global (Figure S5 (a) in the SM) and

376   continental land SSR (Figure S5 (b) in the SM) from the SSRI$_{grid}$ and SSRIH$_{grid}$ (except for Antarctica)

377   during 1955-2018. The most prominent change revolves around the adjustment around 1992: the SSR

378   anomalies were systematically adjusted upward from 1987 to 1992, while the SSR anomalies were

379   systematically adjusted downward from 1993 onwards. Thus, there is a significant decreasing trend for

380   both global land SSRI$_{grid}$ (-1.995±0.251 W/m^2 per decade) and global land SSRIH$_{grid}$ (-1.776±0.230

381   W/m^2 per decade) (except for Antarctica) from 1955 to 1991. While the increasing trend of the global

382   land SSRIH$_{grid}$ from 1991 to 2018 is 0.851±0.410 W/m^2 per decade, slightly smaller than the increasing

383   trend of the SSRI$_{grid}$ (0.999±0.504 W/m^2 per decade). It is worth noting that 1992 happened to be the

384   second year of the eruption of Mount Pinatubo, and the homogenized SSR data integrated in this paper

385   may be affected by this event. But overall, the homogenization also has limited effects on the global SSR

386   variations from Figure S5 (see in the SM), which is consistent with the influence of data homogenization

387   on a wide range of surface air temperatures (Brohan et al., 2006; Xu et al., 2013).

388   At the regional scale, the differences between the SSRIH$_{grid}$ and SSRI$_{grid}$ are more pronounced in Asia

389   and Europe (see Figure S5(b)in the SM). Asia's homogenized SSR show that the regional average SSR

390   has been declining significantly over the period 1958-90; this dimming trend mostly diminished over the

391   period 1991-2005 and was replaced by a brightening trend in the recent decade. The SSRIH$_{grid}$ in Asia is

392   higher than the SSRI$_{grid}$ from 1985 to 1990 and lower than the SSRI$_{grid}$ from 2012 to 2015. The SSRIH$_{grid}$

393   shows a more moderate short-term increase in Europe from 1960 to 1980. Note also that the Australian

394   raw data prior to 1988 were artificially detrended because at the time the Australia Weather Service was

395   afraid that the instruments would drift. Therefore, they detrended them and unfortunately did not store

396   the raw data, and the SSR evolution in Australia is artificial with no trend (Wild et al., 2005). In addition,

397   the SSRI$_{station}$ and SSRIH$_{station}$ comparisons for all 66 stations are shown in Figure S1 (see in the SM).

 5 AI reconstruction and comparison

399 **5.1 Training of the AI model**

400   We produce two (20CRv3 /CMIP6) separate training and validation sets: we select the 1th member

401 data of the reanalysis data and the model data, respectively, as the validation set, and the remaining 79

402 (124) ensemble members as the training sets, where each ensemble member included 732 (720) months

403 of SSR data. Each validation set included 732 (720) samples, while the training sets contained 57828

404 (89280) ensemble members. All the above data, including the *in-situ* observations, are then resampled to

405 monthly anomalies of $5° \times 2.5°$.

406 We reconstruct the SSR of 20CRv3 /CMIP6 with missing values based on 20CRv3 /CMIP6 datasets

407 using the method in section 3.2 and obtain two reconstructions, SSR_{20CR} and SSR_{CMIP6}, respectively. The

408 SSR of 20CRv3/CMIP6 with missing values uses the $SSRIH_{grid}$ mask between 1955 and 2015 /2014. We

409 compare the global land (except for Antarctica) /regional annual anomalies variation of SSR_{20CR}

410 /SSR_{CMIP6}. The results show that SSR_{20CR} is significantly more consistent with the validation set than

411 SSR_{CMIP6}.

412   Figure 6(a) shows that the RMSE/CC of the SSR_{20CR} (0.247 W/m^2 /0.970 W/m^2) are smaller /larger

413 than those of SSR_{CMIP6} (0.518 W/m^2 /0.937 W/m^2) with the original 20CR /CMIP6 dataset. The 20CR-

414 AI model has a better reconstruction ability for SSR at the global land (except for Antarctica) scale. The

415 RMSEs of the SSR_{20CR} (SSR_{CMIP6}) are 1.460 (2.413) W/m^2, 1.109 (1.829) W/m^2, 2.219 (2.596) W/m^2

416 and 1.286 (2.235) W/m^2 in North America, Europe, Asia, and Northern Hemisphere, whereas these

417 values are 1.116 (1.766) W/m^2, 0.622 (1.602) W/m^2, 1.877 (1.839) W/m^2 and 0.772 (1.679) W/m^2 in

418 South America, Africa, Australia, and Southern Hemisphere concerning the original 20CR /CMIP6

419 dataset, respectively. In other words, the RMSEs of the SSR_{20CR} are smaller than those of $SSR_{CMIP6}$for

420 the original 20CR /CMIP6 dataset except for Australia. In addition, the CCs of the SSR_{20CR} (SSR_{CMIP6})

421 are 0.958 (0.830) W/m^2, 0.958 (0.987) W/m^2, 0.886 (0.669) W/m^2, 0.930 (0.965) W/m^2, 0.938 (0.930)

422 W/m^2, 0.943 (0.916) W/m^2, 0.936 (0.875) W/m^2 and 0.903 (0.822) W/m^2 in North America, Europe,

423 Asia, Northern Hemisphere, South America, Africa, Australia, and Southern Hemisphere with respect

424 to the original 20CR /CMIP6 dataset, respectively. That is, the CCs of the SSR_{20CR} are larger than those

425 of $SSR_{CMIP6}$to the original 20CR /CMIP6 dataset except for Europe.

426   Based on the above comparison, the higher uncertainty for CMIP6 model output possibly biases the

427   CMIP6-AI method. Thus, the accuracy of the SSR_{20CR} is higher than that of the SSR_{CMIP6} at both global

428   land (except for Antarctica) and regional scales. Therefore, we choose the reconstruction results of the

429   20CR-AI model as the final AI reconstruction dataset, and subsequent analysis in the following sections

430   is only based on this dataset.

431   **5.2 Comparison of the spatial and temporal variation characteristics**

432   We investigate the long-term trends and spatial and temporal variation of the $SSRIH_{20CR}$, compare the

433   differences between the $SSRIH_{20CR}$ and $SSRIH_{grid}$, and suggest: the area and magnitude of the high and

434   low centres of the $SSRIH_{20CR}$ are the same as those of the $SSRIH_{grid}$; the results of the global land (except

435   for Antarctica) reconstruction are consistent with "dimming and brightening"; the global dimming is

436   primarily dominated by decreasing trends in Asia, Europe Africa and North America, whereas Europe

437   and North America are contributors to the increasing trends.

438   Figure 7 shows the spatial distribution of the $SSRIH_{grid}$ and $SSRIH_{20CR}$ for the three months (July 1960,

439   July 1980, and July 2000). Figure S6 (see in the SM) displays the spatial distribution of annual $SSRIH_{grid}$

440   and $SSRIH_{20CR}$ from 1955 to 2018. Figure 7 also shows the area and the magnitude of the high and low

441   centres in the $SSRIH_{20CR}$ are the same as in the $SSRIH_{grid}$. The $SSRIH_{20CR}$ is mainly positive anomalies

442   in Africa and the Eurasian continent in July 1960, especially in India and the Middle East. Afterwards,

443   India showed a continuous and steady decline in SSR. This confirms the well-known phenomenon of

444   global dimming over India (Wild et al., 2009; Soni et al., 2016; Soni et al., 2012; Padma Kumari et al.,

445   2007; Kambezidis et al., 2012). In Australia, the $SSRIH_{20CR}$ is dominated by negative anomalies in July

446   1980 and positive anomalies in July 1960 and July 2000. In Greenland, the $SSRIH_{20CR}$ shows a large

447   positive anomaly during three months. In northern Russia, there is a high value in July 2000. The

448   reconstruction can better reflect the anomaly distribution of observation information, and the grid boxes

449   with the missing values are infilled and reconstructed, which has high reliability.

450   Figure 8 illustrates global land (except for Antarctica) annual anomalies variation and long-term trend

451   of the $SSRIH_{20CR}$ for the period of 1955-2018, 1955-1991 and 1991-2018. Table S3 in the SM

452   demonstrates the trends of global SSR change evaluation for various data sources on different scales.

453   Also, we compare the differences between the $SSRIH_{20CR}$ and $SSRIH_{grid}$. The minimum value of the

454    $SSRIH_{20CR}$ occurred in 1991 (-2.411 W/m^2). The decreasing trend of the $SSRIH_{20CR}$ from 1955 to 1991

455   (-1.276±0.205 W/m^2 per decade) is slightly lower than that of the $SSRIH_{grid}$ (-1.776±0.230 W/m^2 per

456   decade). After that, the $SSRIH_{20CR}$ turns to an increasing trend of 0.697 ± 0.359 W/m^2 per decade from

457   1991 to 2018. This suggests that the difference between $SSRIH_{20CR}$ and $SSRIH_{grid}$ may be caused by the

458   results observed in limited data coverage (such as in Africa and North America) (Figure 9). After

459   homogenization and reconstruction, the trend (-1.276 W/m^2 per decade) from 1955 to 1991 corresponds

460   to an overall reduction of -4.6 W/m^2 over the dimming period, while that (0.697 W/m^2per decade) from

461   1991 to 2018 correspond to an overall increase of 2 W/m^2 over the brightening period. This is in amazing

462   agreement with the -4 W/m^2 for the dimming period and the 2 W/m^2 for the brightening period based on

463   an overall surface energy budget assessment ((Wild, 2012) see their Figure 1). Also, similar conclusions

464   (incomplete coverage of observational data lead to an underestimation of global warming trends) have

465   been confirmed in global warming research (Gulev et al., 2021; Li et al., 2021).

466   Figure 9 demonstrates the long-term annual anomaly variations of the $SSRIH_{20CR}$ in different regions

467   and its results compared to the $SSRIH_{grid}$. Table S4 in the SM shows the evaluation in continental and

468   hemispheric $SSRIH_{20CR}$ change trends on different scales. The $SSRIH_{20CR}$ shows a similar annual

469   anomaly variation to the global land (except for Antarctica) average trend in North America and Asia,

470   reaches a minimum in the late 1970s or early 1990s, and follows a moderate reversal. In Europe, the

471     $SSRIH_{20CR}$ shows a decrease (-2.180 $\pm$ 1.866 W/m^2 per decade) between 1963 and 1978 before turning

472   to brightening (1.081 $\pm$ 0.312 W/m^2 per decade). In South America and Australia (Southern Hemisphere),

473   the $SSRIH_{20CR}$ shows no significant variation. In Africa, the $SSRIH_{20CR}$ has a dimming trend (-1.506 $\pm$

474   0.496 W/m^2 per decade) from the 1950s to the 1990s, after which it remains levelled off (0.340 $\pm$ 0.998

475   W/m^2 per decade). The $SSRIH_{20CR}$ shows a decreasing trend (-1.457 $\pm$ 0.246 W/m^2 per decade) until the

476   1990s in the Northern Hemisphere and a brightening (0.887 $\pm$ 0.415 W/m^2 per decade) afterwards. The

477   annual average anomaly variations in regions and globally show that Asia, Africa, Europe and North

478   America are the four contributors to the global dimming, while Europe and North America are two major

479   contributors to the "brightening". This is in general agreement with the results obtained by previous

480   machine learning (Yuan et al., 2021). In addition, the discrepancy between the $SSRIH_{20CR}$ and $SSRIH_{grid}$

481   is more significant in low-coverage areas (right) than in high-coverage regions (left). It is particularly

482   pronounced before 1980 and in South America. This suggests that the limited surface observations are

483   not representative of the continental variation in SSR.

484   To sum up, the AI reconstruction of this paper helps to decrease the uncertainties in SSR variations in

485 both spatial scales. Further, it shows that there may be a sampling error in the variations of the global

486 land (except for Antarctica) and regional SSR before reconstruction, leading to a systematic deviation in

487 the long-term trend of global land (except for Antarctica) or regional SSR.

488 **6 Data availability**

489 Both the $SSRIH_{grid}$ (the homogenized monthly gridded SSR data over 1923-2020) and the $SSRIH_{20CR}$

490 (the monthly 20CR-AI model reconstructed SSR data for 1955-2018) are currently publicly available on

491 the figshare website under DOI at https://doi.org/10.6084/m9.figshare.21625079.v1 (Jiao and Li, 2023).

492 These datasets are also available at http://www.gwpu.net for free.

493 **7 Conclusion**

494 In this study, we integrate global station observations based on the raw observational SSRs from GEBA

495 and WRDC, combined with existing homogenized SSR datasets from other scholars. Also, we

496 homogenize the globally distributed station data using the RHtestV4 software package. An improved

497 CNN deep learning algorithm is subsequently used to reconstruct the SSR anomalies. Thus, a

498 reconstructed SSR anomaly dataset, $SSRIH_{20CR}$, is obtained based on training sets (20CRv3), for the

499 years 1955-2018, with a resolution of $5°\times2.5°$. The main results are as follows:

500   1) The first integrated and homogenized global SSR monthly dataset is developed, which contains 944

501 stations in total and covers the longest periods (from the 1920s to recent years). A $5°\times5°$ grid boxes

502 version of the monthly SSR anomalies dataset is derived.

503   2) This paper develops $5°\times2.5°$ full-coverage monthly land (except for Antarctica) SSR anomalies

504 reconstructed datasets based on the above observations, using the 20CRv3 to train the AI model.

505 Comparative validations /evaluations show that the $SSRIH_{20CR}$ provides a reliable benchmark for global

506 SSR variations.

507   3) On average, the global annual SSR variations based on the $SSRIH_{grid}$ are not significantly different,

508 except that the increasing (brightening) trend after 1991 is a little smaller for the latter. The short-term

509 brightening SSR in Europe from the 1970s- to the 1980s disappear at the regional scale. At the same time,

510 the brightening SSR after the 1990s in Asia slowed or postponed.

Author contributions

Boyang Jiao: Software, Data curation, Writing- Original draft preparation, Visualization, Investigation.

Yucheng Su: Software, Data curation.

Qingxiang Li: Methodology, Supervision, Conceptualization, Validation, Writing - Review and Editing.

Veronica Manara: Providing the homogenized Italian dataset, Writing - Review and Editing.

Martin Wild: Writing - Review and Editing.

Competing interests

At least one of the (co-) authors is a member of the editorial board of Earth System Science Data.

Disclaimer

Publisher's note: Copernicus Publications remains neutral about jurisdictional claims in published maps and institutional affiliations.

Financial support

This study is supported by the Natural Science Foundation of China (Grant: 41975105) and the National Key R&D Program of China (Grant: 2018YFC1507705; 2017YFC1502301). The Global Energy Balance Archive (GEBA) is co-funded by the Federal Office of Meteorology and Climatology MeteoSwiss within the framework of GCOS Switzerland. Global dimming and brightening research at ETH Zurich are supported by the Swiss National Science Foundation (Grant No. 200020 188601). Veronica Manara was supported by the "Ministero dell'Università e della Ricerca" of Italy [grant FSE – REACT EU, DM 10/08/2021 n. 1062].

530 **Reference**

531 Aguiar, L. M., Pereira, B., David, M., Díaz, F., and Lauret, P.: Use of satellite data to improve solar

532   radiation forecasting with Bayesian Artificial Neural Networks, Solar Energy, 122, 1309-1324,

533   doi:10.1016/j.solener.2015.10.041, 2015.

534 Alexandersson, H.: A homogeneity test applied to precipitation data, Journal of Climatology, 6, 661-675,

535   doi:10.1002/joc.3370060607, 1986.

536 Bookstein, F. L.: Principal warps: Thin-plate splines and the decomposition of deformations, IEEE

537   Transactions on pattern analysis and machine intelligence, 11, 567-585, doi:10.1109/34.24792, 1989.

538 Brohan, P., Kennedy, J. J., Harris, I., Tett, S. F. B., and Jones, P. D.: Uncertainty estimates in regional and

539   global observed temperature changes: A new data set from 1850, Journal of Geophysical Research:

540   Atmospheres, 111, doi:10.1029/2005JD006548, 2006.

541 Cao, Y., Jiao, B., Lan, X., Tan, J., Yang, Y., Sun, W., Li, Z., Luo, J., and Li, Q.: Reconstruction og China

542   global Merged Surface Temperature (CMST) based on an artifical intelligence approach

543   (submitted), Enviormental Scinence & Technology, 2022.

544 Collins, F. C.: A comparison of spatial interpolation techniques in temperature estimation, The 3rd

545   International Conference/Workshop on Integrating GIS and Environmental Modeling, Santa

546   Barbara, Santa Fe, NM; Santa Barbara, CA, 21-26 January1996 of Conference.

547 Craddock, J. M.: Methods of comparing annual rainfall records for climatic purposes, Weather, 34, 332-

548   346, doi:10.1002/j.1477-8696.1979.tb03465.x, 1979.

549 Driemel, A., Augustine, J., Behrens, K., Colle, S., Cox, C., Cuevas-Agulló, E., Denn, F. M., Duprat, T.,

550   Fukuda, M., and Grobe, H.: Baseline Surface Radiation Network (BSRN): structure and data

551   description (1992–2017), Earth System Science Data, 10, 1491-1501, doi:10.5194/essd-10-1491-

552   2018, 2018.

553 Erxleben, J., Elder, K., and Davis, R.: Comparison of spatial interpolation methods for estimating snow

554   distribution in the Colorado Rocky Mountains, Hydrological Processes, 16, 3627-3649,

555   doi:10.1002/hyp.1239, 2002.

556 Evan, A. T., Heidinger, A. K., and Vimont, D. J.: Arguments against a physical long-term trend in global

557   ISCCP cloud amounts, Geophysical Research Letters, 34, 10.1029/2006gl028083, 2007.

558 Eyring, V., Bony, S., Meehl, G. A., Senior, C. A., Stevens, B., Stouffer, R. J., and Taylor, K. E.: Overview

559  of the Coupled Model Intercomparison Project Phase 6 (CMIP6) experimental design and

560  organization, Geoscientific Model Development, 9, 1937-1958, doi:10.5194/gmd-9-1937-2016,

561  2016.

562 Feng, F. and Wang, K.: Merging high-resolution satellite surface radiation data with meteorological

563  sunshine duration observations over China from 1983 to 2017, Remote Sensing, 13, 602,

564  doi:10.3390/rs13040602, 2021.

565 Fisher, N. I., Lewis, T., and Embleton, B. J.: Statistical analysis of spherical data, Cambridge university

566  press, doi:10.1017/CBO9780511623059, 1993.

567 Fukami, K., Fukagata, K., and Taira, K.: Machine-learning-based spatio-temporal super resolution

568  reconstruction of turbulent flows, Journal of Fluid Mechanics, 909, doi:10.1017/jfm.2020.948, 2021.

569 Gates, W. L., Boyle, J. S., Covey, C., Dease, C. G., Doutriaux, C. M., Drach, R. S., Fiorino, M., Gleckler,

570  P. J., Hnilo, J. J., Marlais, S. M., Phillips, T. J., Potter, G. L., Santer, B. D., Sperber, K. R., Taylor,

571  K. E., and Williams, D. N.: An Overview of the Results of the Atmospheric Model Intercomparison

572  Project (AMIP I), Bulletin of the American Meteorological Society, 80, 29-55, 10.1175/1520-

573  0477(1999)080<0029:Aootro>2.0.Co;2, 1999.

574 Gulev, S. K., Thorne, P. W., J. Ahn, F. J. D., Domingues, C. M., Gerland, S., Gong, D., Kaufman, D. S.,

575  Nnamchi, H. C., Quaas, J., Rivera, J. A., Sathyendranath, S., Smith, S. L., Trewin, B., Shuckmann,

576  K. v., and Vose, R. S.: In: Climate Change 2021: The Physical Science Basis., Climate Change 2021:

577  The Physical Science Basis. Contribution of Working Group I to the Sixth Assessment Report of the

578  Intergovernmental Panel on Climate Change, in, edited by: [Masson-Delmotte, V., Zhai, P., Pirani,

579  A., Connors, S. L., Péan, C., Berger, S., Caud, N., Chen, Y., Goldfarb, L., Gomis, M. I., Huang, M.,

580  Leitzell, K., Lonnoy, E., Matthews, J. B. R., Maycock, T. K., Waterfield, T., Yelekçi, O., Yu, R., and

581  (eds.)], B. Z., Cambridge University Press. 2021., 287–422. Cambridge University Press, 2021.

582 He, J., Hong, L., Shao, C., and Tang, W.: Global evaluation of simulated surface shortwave radiation in

583  CMIP6 models, Atmospheric Research, 292, 10.1016/j.atmosres.2023.106896, 2023.

584 He, Y., Wang, K., and Feng, F.: Improvement of ERA5 over ERA-Interim in simulating surface incident

585  solar radiation throughout China, Journal of Climate, 34, 3853-3867, 2021.

586 Hersbach, H., Bell, B., Berrisford, P., Hirahara, S., Horányi, A., Muñoz-Sabater, J., Nicolas, J., Peubey,

587  C., Radu, R., Schepers, D., Simmons, A., Soci, C., Abdalla, S., Abellan, X., Balsamo, G., Bechtold,

588  P., Biavati, G., Bidlot, J. R., Bonavita, M., Chiara, G. D., Dahlgren, P., Dee, D., Diamantakis, M.,

589   Dragani, R., Flemming, J., Forbes, R. G., Fuentes, M., Geer, A. J., Haimberger, L., Healy, S. B.,

590   Hogan, R. J., Holm, E. V., Janisková, M., Keeley, S. P. E., Laloyaux, P., Lopez, P., Lupu, C., Radnoti,

591   G., Rosnay, P. d., Rozum, I., Vamborg, F., Villaume, S., and Thepaut, J.-N.: The ERA5 global

592   reanalysis, Quarterly Journal of the Royal Meteorological Society, 146, 1999 - 2049,

593   doi:10.1002/qj.3803, 2020.

594   Hoskins, B. J. and Valdes, P. J.: On the existence of storm-tracks, Journal of Atmospheric Sciences, 47,

595   1854-1864, doi:10.1175/1520-0469(1990)047<1854:OTEOST>2.0.CO;2, 1990.

596   Huang, B., Yin, X., Menne, M. J., Vose, R., and Zhang, H.-M.: Improvements to the Land Surface Air

597   Temperature Reconstruction in NOAAGlobalTemp: An Artificial Neural Network Approach,

598   Artificial Intelligence for the Earth Systems, 1-35, doi:10.1175/AIES-D-22-0032.1, 2022.

599   Huang, J., Rikus, L. J., Qin, Y., and Katzfey, J.: Assessing model performance of daily solar irradiance

600   forecasts over Australia, Solar Energy, 176, 615-626, 10.1016/j.solener.2018.10.080, 2018.

601   Jiao, B. and Li, Q.: Global Integrated and Homogenized Solar surface Radiation Datasets,

602   doi:10.6084/m9.figshare.21625079.v1, 2023.

603   Jiao, B., Li, Q., Sun, W., and Martin, W.: Uncertainties in the global and continental surface solar

604   radiation variations: inter-comparison of in-situ observations, reanalyses, and model simulations,

605   Climate Dynamics, 1-18, doi:10.1007/s00382-022-06222-3, 2022.

606   Jones, P., Osborn, T., Briffa, K., Folland, C., Horton, E., Alexander, L., Parker, D., and Rayner, N.:

607   Adjusting for sampling density in grid box land and ocean surface temperature time series, Journal

608   of Geophysical Research: Atmospheres, 106, 3371-3380, doi:10.1029/2000JD900564, 2001.

609   Ju, X., Tu, Q., and Li, Q.: Homogeneity test and reduction of monthly total solar radiation over China, J

610   Nanjing Inst Meteorol, 29, 336-341, 2006.

611   Kadow, C., Hall, D. M., and Ulbrich, U.: Artificial intelligence reconstructs missing climate information,

612   Nature Geoscience, 13, 408-413, doi:10.1038/s41561-020-0582-5, 2020.

613   Kambezidis, H. D., Kaskaoutis, D. G., Kharol, S. K., Moorthy, K. K., Satheesh, S. K., Kalapureddy, M.

614   C. R., Badarinath, K. V. S., Sharma, A. R., and Wild, M.: Multi-decadal variation of the net

615   downward shortwave radiation over south Asia: The solar dimming effect, Atmospheric

616   Environment, 50, 360-372, 2012.

617   Krige, D. G.: A statistical approach to some basic mine valuation problems on the Witwatersrand, Journal

618   of the Southern African Institute of Mining and Metallurgy, 52, 119-139,

619   doi:10.10520/AJA0038223X_4792, 1951.

620 Leirvik, T. and Yuan, M.: A machine learning technique for spatial interpolation of solar radiation

621   observations, Earth and Space Science, 8, e2020EA001527, doi:10.1029/2020EA001527, 2021.

622 Li, Q., Sun, W., Yun, X., Huang, B., Dong, W., Wang, X. L., Zhai, P., and Jones, P.: An updated evaluation

623   of the global mean land surface air temperature and surface temperature trends based on CLSAT

624   and CMST, Climate Dynamics, 56, 635-650, doi: 10.1007/s00382-020-05502-0, 2021.

625 Liang, H., Jiang, B., Liang, S., Peng, J., Li, S., Han, J., Yin, X., Cheng, J., Jia, K., and Liu, Q.: A global

626   long-term ocean surface daily/0.05° net radiation product from 1983–2020, Scientific Data, 9, 1-17,

627   doi:10.1038/s41597-022-01419-x, 2022.

628 Ma, Q., Wang, K., He, Y., Su, L., Wu, Q., Liu, H., and Zhang, Y.: Homogenized century-long surface

629   incident solar radiation over Japan, Earth System Science Data, 14, 463-477, doi:10.5194/essd-14-

630   463-2022, 2022.

631 Manara, V., Bassi, M., Brunetti, M., Cagnazzi, B., and Maugeri, M.: 1990–2016 surface solar radiation

632   variability and trend over the Piedmont region (northwest Italy), Theoretical and Applied

633   Climatology, 136, 849-862, doi:10.1007/s00704-018-2521-6, 2019.

634 Manara, V., Brunetti, M., Celozzi, A., Maugeri, M., Sanchez-Lorenzo, A., and Wild, M.: Detection of

635   dimming/brightening in Italy from homogenized all-sky and clear-sky surface solar radiation

636   records and underlying causes (1959–2013), Atmospheric Chemistry and Physics, 16, 11145-11161,

637   doi:10.5194/acp-16-11145-2016, 2016.

638 Manara, V., Stocco, E., Brunetti, M., Diolaiuti, G. A., Fugazza, D., Pfeifroth, U., Senese, A., Trentmann,

639   J., and Maugeri, M.: Comparison of Surface Solar Irradiance from Ground Observations and

640   Satellite Data (1990–2016) over a Complex Orography Region (Piedmont—Northwest Italy),

641   Remote Sensing, 12, 3882, 2020.

642 Manara., V., Michele., B., ., M. M., ., S.-L. A., and Martin, W.: Homogenization of a surface solar

643   radiation dataset over Italy, AIP Conference Proceedings, 22 February 2017,   doi:

644   org/10.1063/1.4975544, 2017.

645 Mlawer, E. J., Taubman, S. J., Brown, P. D., Iacono, M. J., and Clough, S. A.: Radiative transfer for

646   inhomogeneous atmospheres: RRTM, a validated correlated-k model for the longwave, Journal of

647   Geophysical Research: Atmospheres, 102, 16663-16682, https://doi.org/10.1029/97JD00237, 1997.

648 Olanow, C. W. and Koller, W. C.: An algorithm (decision tree) for the management of Parkinson's disease:

Treatment guidelines, Neurology, 50, S1-s88, 1998.

Padma Kumari, B., Londhe, A. L., Daniel, S., and Jadhav, D. B.: Observational evidence of solar dimming: Offsetting surface warming over India, Geophysical Research Letters, 34, https://doi.org/10.1029/2007GL031133, 2007.

Peixoto, J. P., Oort, A. H., and Lorenz, E. N.: Physics of climate, Springer1992.

Peterson, T. C., Karl, T. R., Jamason, P. F., Knight, R., and Easterling, D. R.: First difference method: Maximizing station density for the calculation of long-term global temperature change, Journal of Geophysical Research: Atmospheres, 103, 25967-25974, doi:10.1029/98JD01168, 1998.

Pfeifroth, U., Sanchez-Lorenzo, A., Manara, V., Trentmann, J., and Hollmann, R.: Trends and Variability of Surface Solar Radiation in Europe Based On Surface- and Satellite-Based Data Records, Journal of Geophysical Research: Atmospheres, 123, 1735-1754, doi: 10.1002/2017JD027418, 2018.

Ronneberger, O., Fischer, P., and Brox, T.: U-net: Convolutional networks for biomedical image segmentation, International Conference on Medical image computing and computer-assisted intervention, 234-241, doi:10.48550/arXiv.1505.04597,

Sanchez-Lorenzo, A., Calbó, J., and Wild, M.: Global and diffuse solar radiation in Spain: Building a homogeneous dataset and assessing their trends, Global and Planetary Change, 100, 343-352, doi:10.1016/j.gloplacha.2012.11.010, 2013a.

Sanchez-Lorenzo, A., Wild, M., and Trentmann, J.: Validation and stability assessment of the monthly mean CM SAF surface solar radiation dataset over Europe against a homogenized surface dataset (1983–2005), Remote sensing of environment, 134, 355-366, doi:10.1016/j.rse.2013.03.012, 2013b.

Sanchez-Lorenzo, A., Wild, M., Brunetti, M., Guijarro, J. A., Hakuba, M. Z., Calbó, J., Mystakidis, S., and Bartok, B.: Reassessment and update of long-term trends in downward surface shortwave radiation over Europe (1939–2012), Journal of Geophysical Research: Atmospheres, 120, 9555-9569, doi:10.1002/2015JD023321, 2015.

Scudiero, E., Corwin, D. L., Morari, F., Anderson, R. G., and Skaggs, T. H.: Spatial interpolation quality assessment for soil sensor transect datasets, Computers and Electronics in Agriculture, 123, 74-79, doi:10.1016/j.compag.2016.02.016, 2016.

Shao, C., Yang, K., Tang, W., He, Y., Jiang, Y., Lu, H., Fu, H., and Zheng, J.: Convolutional neural network-based homogenization for constructing a long-term global surface solar radiation dataset, Renewable and Sustainable Energy Reviews, 169, 10.1016/j.rser.2022.112952, 2022.

679 Shepard, D.: A two-dimensional interpolation function for irregularly-spaced data, Proceedings of the

680   1968 23rd ACM national conference, 517-524,   doi:10.1145/800186.810616,

681 Slivinski, L. C., Compo, G. P., Whitaker, J. S., Sardeshmukh, P. D., Giese, B. S., McColl, C., Allan, R.,

682   Yin, X., Vose, R., and Titchner, H.: Towards a more reliable historical reanalysis: Improvements for

683   version 3 of the Twentieth Century Reanalysis system, Quarterly Journal of the Royal

684   Meteorological Society, 145, 2876-2908, doi:10.1002/qj.3598, 2019.

685 Soni, V. K., Pandithurai, G., and Pai, D. S.: Evaluation of long-term changes of solar radiation in India,

686   International Journal of Climatology, 32, 540-551, https://doi.org/10.1002/joc.2294, 2012.

687 Soni, V. K., Pandithurai, G., and Pai, D. S.: Is there a transition of solar radiation from dimming to

688   brightening over India, Atmospheric Research, 169, 209-224, 2016.

689 Tang, W., Yang, K., Qin, J., Li, X., and Niu, X.: A 16-year dataset (2000–2015) of high-resolution (3 h,

690   10 km) global surface solar radiation, Earth System Science Data, 11, 1905-1915, doi:10.5194/essd-

691   11-1905-2019, 2019.

692 Tang, W., Qin, J., Yang, K., Liu, S., Lu, N., and Niu, X.: Retrieving high-resolution surface solar radiation

693   with cloud parameters derived by combining MODIS and MTSAT data, Atmospheric Chemistry

694   and Physics, 16, 2543-2557, doi:10.5194/acp-16-2543-2016, 2016.

695 Trenberth, K. E. and Fasullo, J. T.: Regional energy and water cycles: Transports from ocean to land,

696   Journal of Climate, 26, 7837-7851, doi:10.1175/JCLI-D-13-00008.1, 2013.

697 Tsvetkov, A., Wilcox, S., Renne, D., and Pulscak, M.: International solar resource data at the World

698   Radiation Data Center, American Solar Energy Society, Boulder, CO (United States), 1995.

699 Urraca, R., Huld, T., Martinez-de-Pison, F. J., and Sanz-Garcia, A.: Sources of uncertainty in annual

700   global horizontal irradiance data, Solar Energy, 170, 873-884, 10.1016/j.solener.2018.06.005, 2018.

701 Vincent, L. A., Wang, X. L., Milewska, E. J., Wan, H., Yang, F., and Swail, V.: A second generation of

702   homogenized Canadian monthly surface air temperature for climate trend analysis, Journal of

703   Geophysical Research: Atmospheres, 117, doi:10.1029/2012JD017859, 2012.

704 Wang, K.: Measurement biases explain discrepancies between the observed and simulated decadal

705   variability of surface incident solar radiation, Scientific reports, 4, 1-7, doi:0.1038/srep06144 2014.

706 Wang, K., Ma, Q., Li, Z., and Wang, J.: Decadal variability of surface incident solar radiation over China:

707   Observations, satellite retrievals, and reanalyses, Journal of Geophysical Research: Atmospheres,

708   120, 6500-6514, doi:10.1002/2015JD023420, 2015.

709   Wang, X. L.: Accounting for autocorrelation in detecting mean shifts in climate data series using the

710   penalized maximal t or F test, Journal of applied meteorology and climatology, 47, 2423-2444,

711   doi:10.1175/2008JAMC1741.1, 2008a.

712   Wang, X. L.: Penalized maximal F test for detecting undocumented mean shift without trend change,

713   Journal of Atmospheric and Oceanic Technology, 25, 368-384, doi:10.1175/2007JTECHA982.1,

714   2008b.

715   Wang, X. L. and Feng, Y.: RHtestsV4 user manual, Climate Research Division, Atmospheric Science and

716   Technology Directorate, Science and Technology Branch, Environment Canada, 28, 2013.

717   Wang, X. L., Wen, Q. H., and Wu, Y.: Penalized maximal t test for detecting undocumented mean change

718   in climate data series, Journal of Applied Meteorology and Climatology, 46, 916-931,

719   doi:10.1175/JAM2504.1, 2007.

720   Wang, X. L., Chen, H., Wu, Y., Feng, Y., and Pu, Q.: New techniques for the detection and adjustment of

721   shifts in daily precipitation data series, Journal of Applied Meteorology and Climatology, 49, 2416-

722   2436, doi:10.1175/2010JAMC2376.1, 2010.

723   Wang, Y. and Wild, M.: A new look at solar dimming and brightening in China, Geophysical Research

724   Letters, 43, 11,777-711,785, doi:10.1002/2016GL071009, 2016.

725   Wild, M.: Enlightening global dimming and brightening, Bulletin of the American Meteorological

726   Society, 93, 27-37, doi:10.1175/BAMS-D-11-00074.1, 2012.

727   Wild, M.: The global energy balance as represented in CMIP6 climate models, Clim Dyn, 55, 553-577,

728   10.1007/s00382-020-05282-7, 2020.

729   Wild, M., Trüssel, B., Ohmura, A., Long, C. N., König-Langlo, G., Dutton, E. G., and Tsvetkov, A.:

730   Global dimming and brightening: An update beyond 2000, Journal of Geophysical Research:

731   Atmospheres, 114, https://doi.org/10.1029/2008JD011382, 2009.

732   Wild, M., Ohmura, A., Schär, C., Müller, G., Folini, D., Schwarz, M., Hakuba, M. Z., and Sanchez-

733   Lorenzo, A.: The Global Energy Balance Archive (GEBA) version 2017: A database for worldwide

734   measured surface energy fluxes, Earth System Science Data, 9, 601-613, doi:10.5194/essd-9-601-

735   2017, 2017.

736   Wild, M., Gilgen, H., Roesch, A., Ohmura, A., Long, C. N., Dutton, E. G., Forgan, B., Kallis, A., Russak,

737   V., and Tsvetkov, A.: From dimming to brightening: Decadal changes in solar radiation at Earth's

738   surface, Science, 308, 847-850, doi:10.1126/science.1103215, 2005.

739 Xu, W., Li, Q., Wang, X. L., Yang, S., Cao, L., and Feng, Y.: Homogenization of Chinese daily surface

740   air temperatures and analysis of trends in the extreme temperature indices, Journal of Geophysical

741   Research: Atmospheres, 118, 9708-9720, doi:10.1002/jgrd.50791, 2013.

742 Xu, W., Li, Q., Jones, P., Wang, X. L., Trewin, B., Yang, S., Zhu, C., Zhai, P., Wang, J., and Vincent, L.:

743   A new integrated and homogenized global monthly land surface air temperature dataset for the

744   period since 1900, Climate Dynamics, 50, 2513-2536, doi:10.1007/s00382-017-3755-1, 2018.

745 Yang, L., Zhang, X., Liang, S., Yao, Y., Jia, K., and Jia, A.: Estimating surface downward shortwave

746   radiation over China based on the gradient boosting decision tree method, Remote Sensing, 10, 185,

747   doi:10.3390/rs10020185, 2018a.

748 Yang, S.: Chinese Monthly homogenized   surface solar radiation datasets (V 1.0), 2016.

749 Yang, S., Wang, X. L., and Wild, M.: Homogenization and trend analysis of the 1958–2016 in situ surface

750   solar radiation records in China, Journal of Climate, 31, 4529-4541, doi:10.1175/JCLI-D-17-0891.1,

751   2018b.

752 You, Q., Sanchez-Lorenzo, A., Wild, M., Folini, D., Fraedrich, K., Ren, G., and Kang, S.: Decadal

753   variation of surface solar radiation in the Tibetan Plateau from observations, reanalysis and model

754   simulations, Climate dynamics, 40, 2073-2086, doi:10.1007/s00382-012-1383-3, 2013.

755 Yuan, M., Leirvik, T., and Wild, M.: Global trends in downward surface solar radiation from spatial

756   interpolated ground observations during 1961–2019, Journal of Climate, 34, 9501-9521,

757   doi:10.1175/JCLI-D-21-0165.1, 2021.

758 Zhou, C., He, Y., and Wang, K.: On the suitability of current atmospheric reanalyses for regional warming

759   studies over China, Atmospheric Chemistry and Physics, 18, 8113-8136, 10.5194/acp-18-8113-

760   2018, 2018a.

761 Zhou, C., Wang, K., and Ma, Q.: Evaluation of Eight Current Reanalyses in Simulating Land Surface

762   Temperature from 1979 to 2003 in China, Journal of Climate, 30, 7379-7398,

763   https://doi.org/10.1175/JCLI-D-16-0903.1, 2017.

764 Zhou, W., Gong, L., Wu, Q., Xing, C., Wei, B., Chen, T., Zhou, Y., Yin, S., Jiang, B., Xie, H., Zhou, L.,

765   and Zheng, S.: Correction to: PHF8 upregulation contributes to autophagic degradation of E-

766   cadherin, epithelial-mesenchymal transition and metastasis in hepatocellular carcinoma, Journal of

767   Experimental & Clinical Cancer Research, 37, 10.1186/s13046-018-0944-7, 2018b.

768 Zhou, W., Gong, L., Wu, Q., Xing, C., Wei, B., Chen, T., Zhou, Y., Yin, S., Jiang, B., Xie, H., Zhou, L.,

769	and Zheng, S.: Correction to: PHF8 upregulation contributes to autophagic degradation of E-

770	cadherin, epithelial-mesenchymal transition and metastasis in hepatocellular carcinoma, J Exp Clin

771	Cancer Res, 38, 445, 10.1186/s13046-019-1452-0, 2019.

772

Captions of tables and Figures

Table 1: List of information on the various types of data used in this paper.

Figure 1: Flowchart of quality control (QC) (first step), homogenization (second step) and integration (third step).

Figure 2: Spatial distribution of candidate stations ("*") and added stations ("+"). The different colour bars represent the length of the station record in months (Units: Month).

Figure 3: Spatial distribution of stations after homogenization (Units: Month), different colours represent the length of station records in months

Figure 4: Flowchart of AI reconstruction.

Figure 5: (a) Spatial distribution of $5°x5°$grid boxes ($SSRIH_{grid}$) obtained interpolating the homogenized global land (except for Antarctica) SSR series. The different colours represent the length (the sum of all records) of the station record, Units: Year. (b) Grid box coverage for the homogenized global land (except for Antarctica) SSR ($SSRIH_{grid}$) except for Antarctica.

Figure 6: Reconstruction capabilities of the AI model.

Figure 7: Spatial distribution of the $SSRIH_{grid}$ (a1-3) and $SSRIH_{20CR}$ (b1-3) in typical months. 1-3 is July 1960, July 1980, and July 2000, respectively.

Figure 8: Global land (except for Antarctica) time series of the annual anomaly variations SSR (relative to 1971-2000) before/after reconstruction.

Figure 9: Same as Figure 8, but for regional annual anomaly variations.

803 **Table 1: List of information on the various types of data used in this paper**

	Abbreviation	Resolution	Time	Reference
In-situ-Raw	GEBA (Station)	Monthly	1922-2020	(Wild et al., 2017)
	WRDC (Station)	Monthly	1964-2017	(Tsvetkov et al., 1995)
In-situ-Homo	China (Station)	Monthly	1950-2016	(Yang et al., 2018b)
	Japan (Station)	Monthly	1870-2015	(Ma et al., 2022)
	Europe (Station)	Monthly	1922-2012	(Sanchez-Lorenzo et al., 2015)
	Italy (Station)	Monthly	1959-2016	(Manara et al., 2016; Manara et al., 2019)
Reanalysis / Model	ERA5 (Grid)	Monthly/ $0.25°\times0.25°$	1950-2020	(Hersbach et al., 2020)
	20CRv3 (Grid)	Monthly/ $0.7°\times0.7°$	1940-2015	(Slivinski et al., 2019)
	CMIP6 (Grid)	Monthly/-	1940-2014	(Eyring et al., 2016)

804
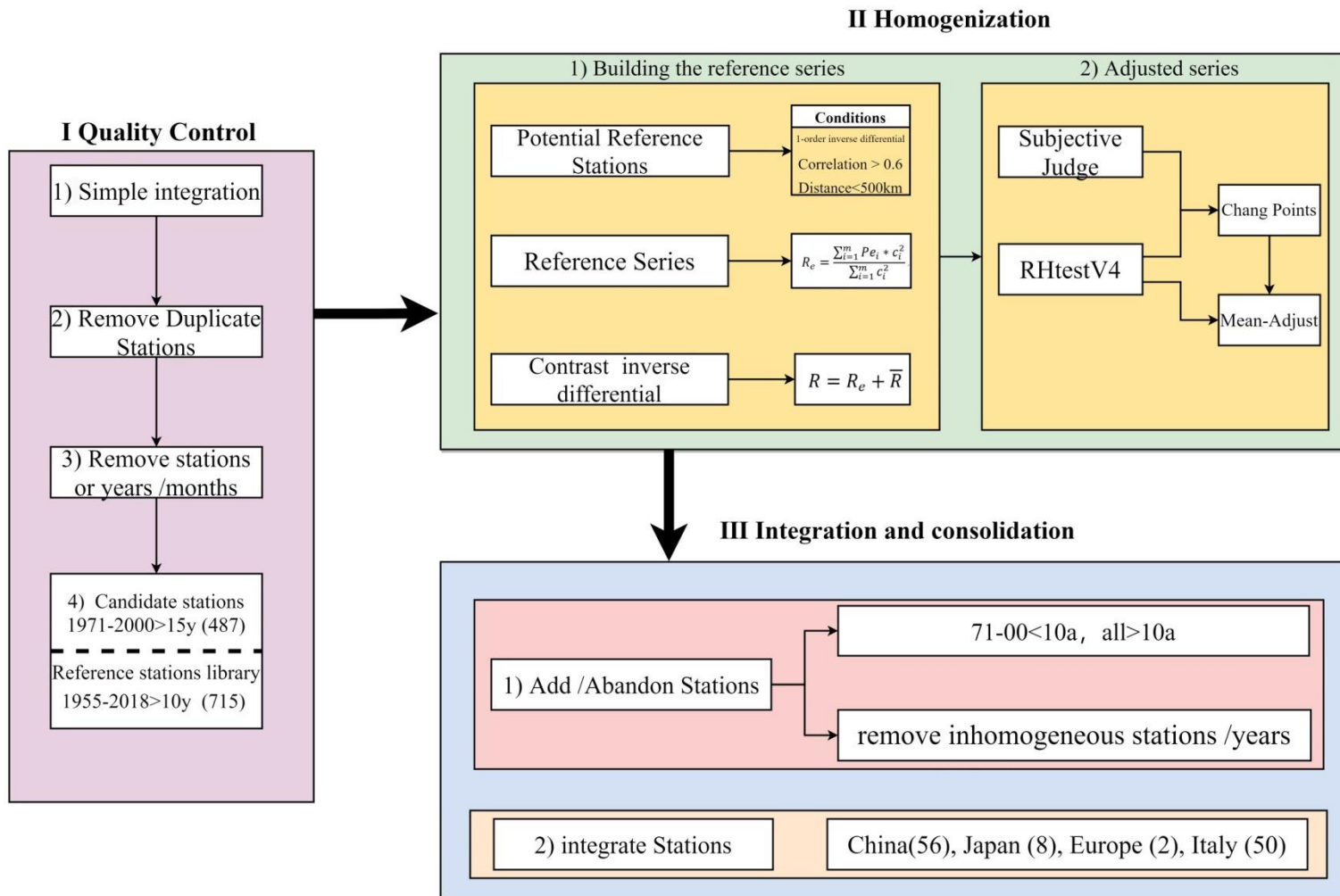
805

806   **Figure 1: Flowchart of quality control (QC) (first step), homogenization (second step) and integration (third step).**
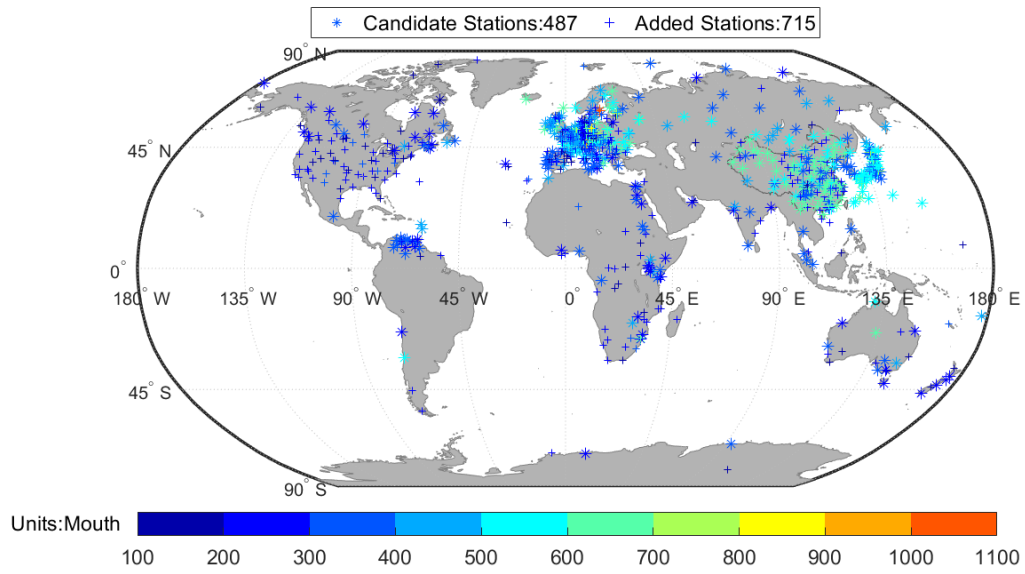
807

808 **Figure 2: Spatial distribution of candidate stations ("*") and added stations ("+"). The different colour bars**
809 **represent the length of the station record in months (Units: Month).**
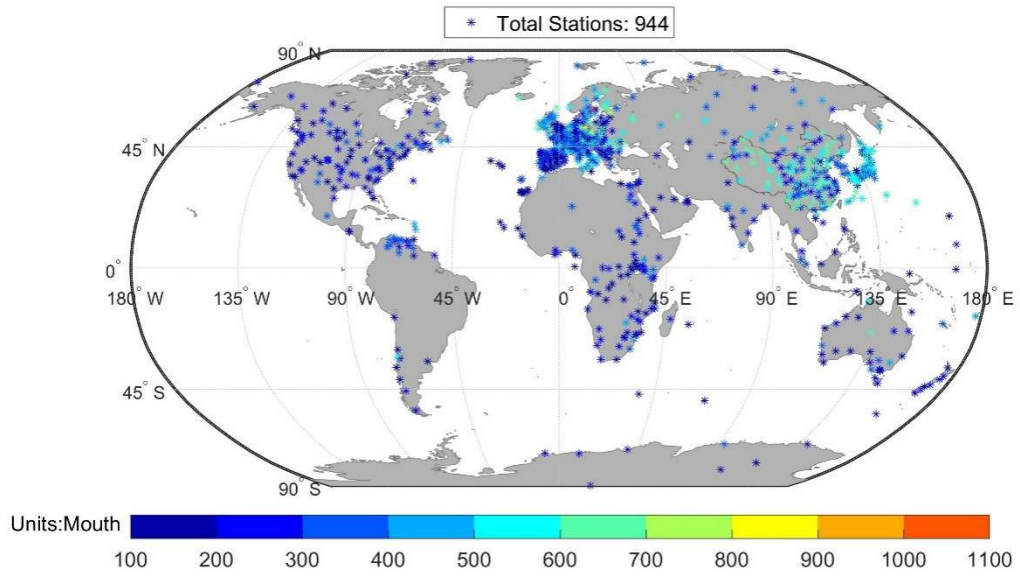
810
811 **Figure 3: Spatial distribution of stations after homogenization (Units: Month), different colours represent the**

812 **length of station records in months.**
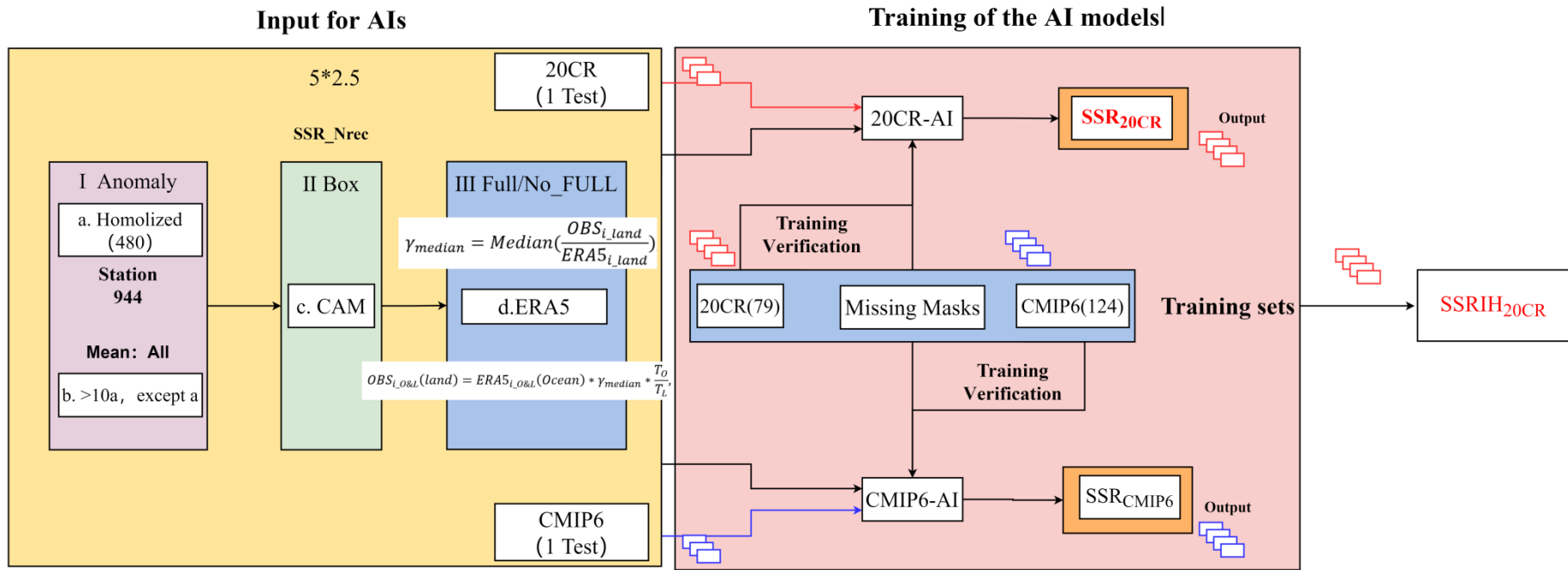
813

814 **Figure 4: Flowchart of AI reconstruction.**

815

816
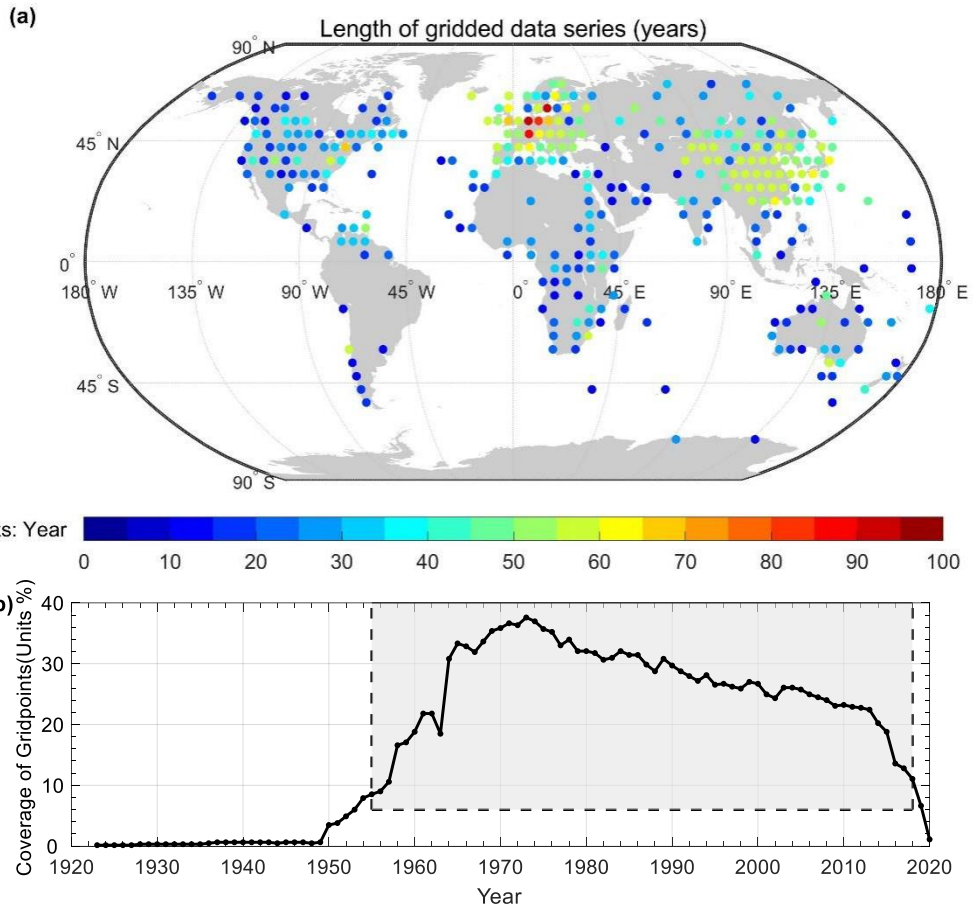
Figure 5: (a) Spatial distribution of 5°×5°grid boxes (SSRIH$_{grid}$) obtained interpolating the homogenized global land (except for Antarctica) SSR series. The different colours represent the length (the sum of all records) of the station record, Units: Year. (b) Grid box coverage for the homogenized global land (except for Antarctica) SSR (SSRIH$_{grid}$) except for Antarctica.

821

822
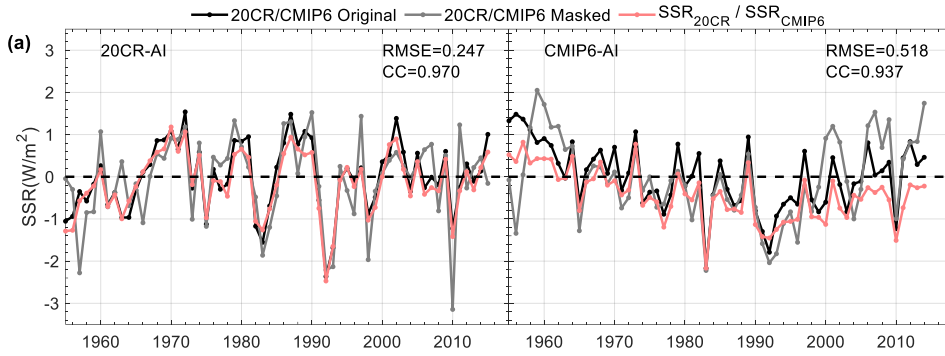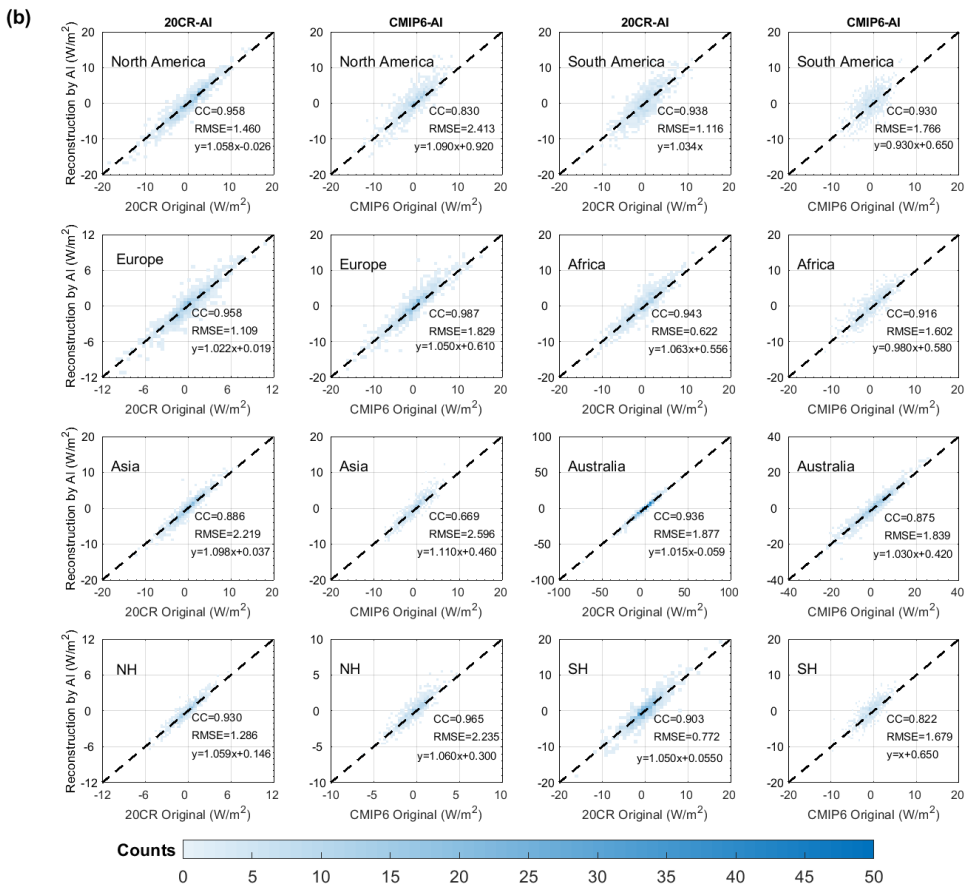
Figure 6: Reconstruction capabilities of the AI model. (a) Global land (except for Antarctica) means time-series analysis and AI model reconstruction evaluation. The red line is the SSR of the reconstruction based on the 20CR-AI /CMIP6-AI model (SSR$_{20CR}$ /SSR$_{CMIP6}$); The grey line is the masked datasets with missing values of the SSRIH$_{grid}$. The solid black line is the 20CR and CMIP6 validation set (the SSR from the 1th member of 20CRv3 /CMIP6). (b) Comparisons of the SSR$_{20CR}$ (columns 1, 3) /SSR$_{CMIP6}$ (columns 2, 4) with the SSR from the 20CR and CMIP6 validation set. Colour bars represent counts with the same values for both. Figures also show the SSR$_{20CR}$ (SSR$_{CMIP6}$) correlation coefficient (CC), root mean squared error (RMSE) and fitting equation compared to the original dataset in different regions.

831
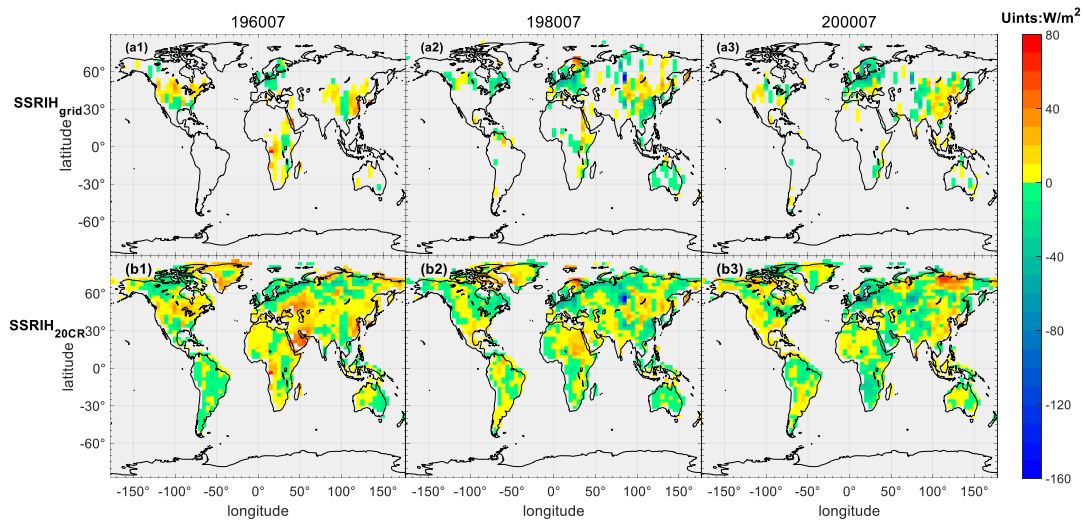
Figure 7: Spatial distribution of the SSRIH$_{grid}$ (a1-3) and SSRIH$_{20CR}$ (b1-3) in typical months. 1-3 is July 1960, July 1980, and July 2000, respectively.
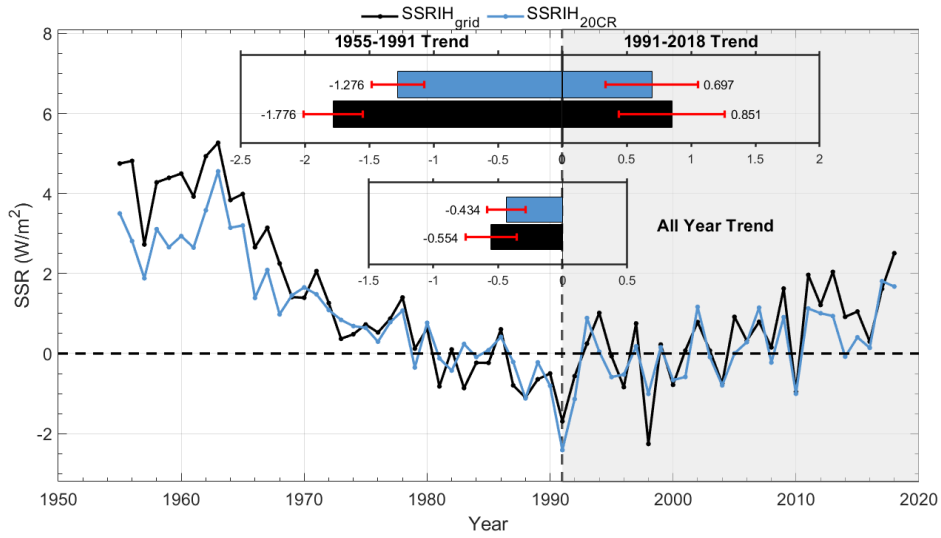
834

835 **Figure 8: Global land (except for Antarctica) annual SSR anomaly variations (relative to 1971-2000)**

836 **before/after reconstruction. The Black solid line represents the SSRIH$_{grid}$ annual anomalies. The solid blue**

837 **line represents the SSRIH$_{20CR}$ annual anomalies. The histograms represent the decadal trends of the**

838 **SSRIH$_{grid}$ /SSRIH$_{20CR}$ (unit: W/m^2 per decade) and their 95% uncertainty range from 1955 to 1991, 1991-**

839 **2018 and 1955-2018.**

840
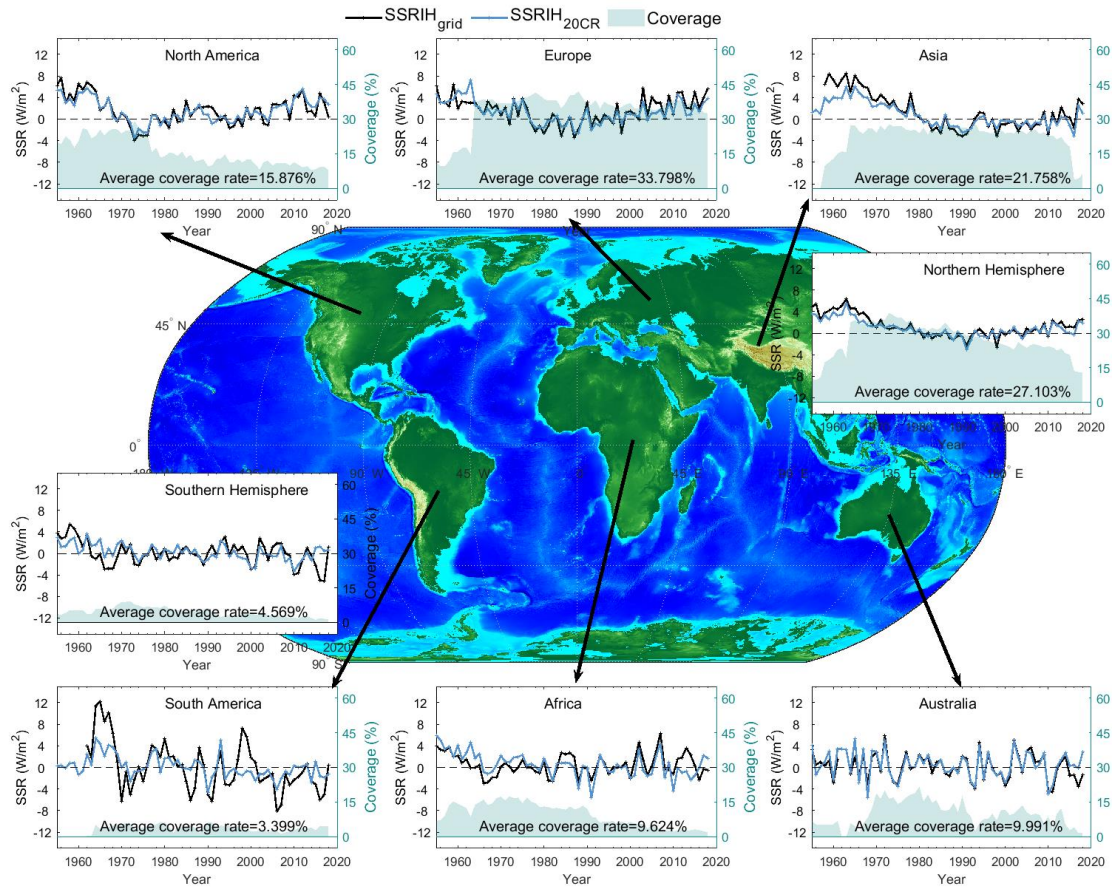
Figure 9: Same as Figure 8, but for regional annual anomaly variations. The green colour filling diagram represents the variation in grid box coverage (before reconstruction).